UAV image sequence reveals feature damage during hurricane evolution

Bo Liu¹, Xiongwu Xiao¹, Zhenfeng Shao¹, Yingbing Li², Shinying Dai², Wenxin Fu², Deren Li¹

¹ State Key Laboratory of Information Engineering in Surveying, Mapping and Remote Sensing (LIESMARS), Wuhan University, Wuhan 430072, China – (trifurs, xwxiao, shaozhenfeng, drli)@whu.edu.cn

Keywords: UAV, Hurricane, Damage assessment, Semantic segmentation, Spatial analysis.

Abstract

In recent years, hurricane disasters have occurred frequently, causing significant losses to human society. UAV technology, with its advantages of high mobility and low cost, has been widely applied in post-disaster loss assessment. However, existing UAV image assessment methods still exhibit deficiencies in model accuracy and the rapid analysis of spatial distribution of disaster events. To address these issues, this study proposes a semantic segmentation model, H4DNet, which combines the global feature extraction capability of SegFormer and the information reconstruction capability of U-Net, aiming to efficiently extract information about damaged objects from UAV images. Experimental results show that H4DNet achieved a 93.71% average accuracy, 87.80% mean accuracy, and 78.01% mean Intersection over Union (mIoU) on the RescueNet dataset, outperforming other comparative models. Furthermore, this paper introduces the Disaster Damage Index (DDI), which generates a spatial distribution map of disaster events by calculating the area proportion of damaged objects and using an Adjusted Inverse Distance Weighting (AIDW) spatial interpolation algorithm. The results indicate that DDI can accurately reflect the severity of disaster-affected areas. The study also verified the energy attenuation process after hurricane landfall through the spatial distribution of objects affected by different disaster levels, providing valuable insights for disaster assessment and emergency response.

1. Introduction

In recent years, the frequency and severity of natural disasters have been increasing, causing significant impacts on both human society and the natural environment (Markhvida et al. 2020; Opper, Park and Husted 2023). Over the past few decades, various types of natural disasters have resulted in approximately 40,000 to 50,000 deaths annually and displaced millions of people (Ritchie et al., 2022). Among these, hurricanes are particularly destructive due to their wide-ranging impacts and potential to trigger secondary disasters such as floods and debris flows, making them one of the most devastating natural hazards. In the aftermath of such events, the rapid acquisition of detailed information about the affected areas is crucial for formulating effective emergency response strategies and post-disaster recovery plans (Fan et al., 2017). However, traditional groundbased survey methods are often time-consuming, costly, and pose safety risks to field personnel due to the complex and hazardous conditions in disaster-stricken areas.

From a bibliometric perspective, researchers have proposed two emerging approaches to obtain post-disaster information on building damage, road blockages, and the status of critical infrastructure, while ensuring personnel safety. The first is the social media-based approach, which establishes functional relationships between the volume and frequency of social media posts and the extent of disaster damage (Guan and Chen, 2014), or employs natural language processing and computer vision techniques to extract useful disaster-related information from text and images (Christidou et al., 2022). However, the completeness and accuracy of social media data can be unreliable. The second is the satellite remote sensing approach, which leverages the monitoring capabilities of remote sensing satellites to acquire real-time imagery of affected areas (Robinson et al., 2023). Advanced image processing techniques

such as object detection and semantic segmentation are then applied to accurately identify and assess damage to buildings and roads. Nevertheless, the effectiveness of disaster assessment using this method is often constrained by weather conditions and the spatial resolution of the imagery (Holail et al., 2024).

Unmanned Aerial Vehicles (UAVs), as a near-ground remote sensing technology, have been increasingly applied in disaster assessment and emergency response due to their high mobility, low cost, and operational flexibility (Cheng et al., 2024; Jozi et al., 2024). In the field of post-disaster damage assessment, UAVs retain the rapid response advantage of social media and the efficiency of satellite remote sensing, while offering greater flexibility and significantly higher spatial resolution. These characteristics substantially enhance the speed and quality of post-disaster response efforts (Cheng et al., 2024). By employing semantic segmentation models, UAVs can automatically analyze and process imagery from disasteraffected areas, segmenting objects such as buildings, roads, and vegetation, and further assessing their levels of damage (Mai et al., 2024). The segmentation results can be used to evaluate road accessibility (Chowdhury et al., 2020) and locate potential survivors (Raja et al., 2024), enabling timely deployment of rescue resources. This is crucial for tracking rescue progress and adjusting emergency response strategies accordingly. In addition, UAVs can conduct frequent flights shortly after a disaster, capturing continuous image data to support real-time monitoring of changes within the affected area (Schaefer et al., 2020).

However, current semantic segmentation models still face several limitations when applied to UAV imagery in postdisaster scenarios. First, the accuracy of these models requires further improvement. Post-disaster images often contain rich information on damage and hazard distribution, which is critical

² School of Geodesy and Geomatics, Wuhan University, Wuhan 430072, China – (ybli, dai.shinying, wenxinw)@whu.edu.cn

for emergency rescue. Damaged buildings and fallen trees, for instance, exhibit less geometric regularity compared to objects in UAV imagery under normal conditions, posing significant challenges for model-based recognition. Moreover, the practical applications of segmented imagery remain underdeveloped. Traditional photogrammetric 3D reconstruction methods are time-consuming and cannot meet the time-sensitive demands of emergency response. Therefore, efficiently obtaining the spatial distribution of objects with varying levels of damage is a fundamental requirement for post-disaster assessment and subsequent recovery efforts.

To address these two challenges, this study proposes a novel model named H4DNet (Hurricane Disaster Damage Detection from Drones), which integrates the U-Net architecture (Ronneberger et al., 2015) with SegFormer (Xie et al., 2021) for semantic segmentation of post-hurricane disaster scenes. H4DNet utilizes a Mix Transformer structure for progressive downsampling, effectively capturing global contextual information and modeling long-range dependencies. The model leverages a hierarchical design to fully exploit multi-scale features, while spatial details are preserved through upsampling and skip connections, ensuring high segmentation accuracy at fine-grained levels. Furthermore, based on the proportion of areas occupied by buildings and roads with different levels of damage in UAV imagery, we introduce a Disaster Damage Index (DDI) to quantitatively describe the severity of the disaster. By mapping the DDI values of each image to their corresponding geographic locations and applying the Adjusted Inverse Distance Weighting (AIDW) method (Zhengquan et al., 2018) for spatial interpolation, the model enables rapid identification of severely affected regions.

2. Methods

2.1 H4DNet: A Novel Semantic Segmentation Model

Architecture of H4DNet: The overall architecture of the H4DNet (Natural Hurricane Disaster Damage Detection from Drones) model is illustrated in the diagram and can be divided into an encoder section and a decoder section, functioning in a top-down and bottom-up manner, respectively. The encoder section is designed based on the SegFormer framework, featuring a hierarchical Mix Transformer for feature extraction. This design enables the model to capture global context through continuous downsampling (Xie et al., 2021). The application of Transformer modules allows the model to effectively handle long-range dependencies while the hierarchical design ensures that features at various scales are fully utilized. The decoder section employs an expansion path similar to U-Net, using upsampling and skip connections to restore spatial information, thereby ensuring detail accuracy (Ronneberger et al., 2015).

Assuming the input is a UAV image of size W×H×3, where H is the height, W is the width, and 3 represents the RGB color channels, the image is first processed through Patch Partition, which divides the image into smaller patches to retain local features and reduce the input data dimensions. The Linear Embedding then converts each image patch into a representation vector suitable for subsequent self-attention mechanisms. A convolutional layer with a stride of 2 is then applied for downsampling, reducing the image size to H/2×W/2×C0, where C0 is the current custom channel number. The data then follows two branches: one branch transfers spatial information to the Decoder via a skip connection, while the

other undergoes 2×2 max pooling, reducing the size to $H/4\times W/4\times C1$ before entering the first Transformer module.

The Transformer module does not alter the feature size, so its output remains $H/4 \times W/4 \times C1$. After passing through a 3×3 convolution, the data flow splits into two branches again, repeating the process of skip connections and downsampling three more times. The encoder section thus generates a series of features at different resolutions. These multi-scale feature maps are then fused together through upsampling and concatenation operations to form a higher-dimensional feature representation.

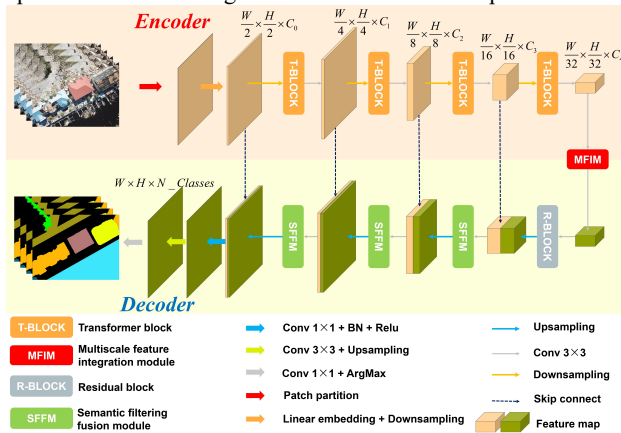


Figure 1. Structure of the H4DNet model.

In the decoder section, the deepest features from the encoder are first upsampled to restore spatial resolution. A key feature of U-Net is its skip connections, which concatenate upsampled feature maps with the corresponding encoder layers. This approach preserves more detailed information. Additionally, the Multiscale Feature Integration Module, Residual Block, and Semantic Filtering Fusion Module are employed to integrate multi-scale features, learn deep features, and refine semantic information, enhancing the model's performance and accuracy. As the decoder progresses, the feature maps gradually restore to the original input size of W×H×N_Classes (where N_Classes represents the number of classes). Each layer involves upsampling and feature concatenation until the original image size is achieved.

2.1.2 Transformer Block Design: Unlike ViT, the encoder of H4DNet can generate multi-scale features, enhancing semantic segmentation performance. Specifically, given an input image of size W×H×3, it produces a series of features at different resolutions:

$$\frac{W}{2^{i+1}} \times \frac{H}{2^{i+1}} \times C_i, \quad i \in \{1, 2, 3, 4\} \text{ and } C_{i+1} > C_i$$
 (1)

As illustrated in Figure 2, the key component of the encoder is a series of Mix Transformer encoders (MiT) modules. This module primarily consists of Efficient Self-Attention, Mix-FFN, and Overlap Patch Merging.

The Efficient Self-Attention module is an improved self-attention mechanism designed to reduce computational complexity and memory usage while maintaining the model's representational power. The input feature map is linearly transformed into three distinct matrices: Query (Q), Key (K), and Value (V).

$$Attention(Q, K, V) = Softmax(\frac{QK^{T}}{\sqrt{d_{band}}})V$$
 (2)

Q, K, and V all have the same dimensions of N×C, where N=W×H. To reduce computational complexity, the length of the features (i.e., N) is reduced through Reshape + Linear layers.

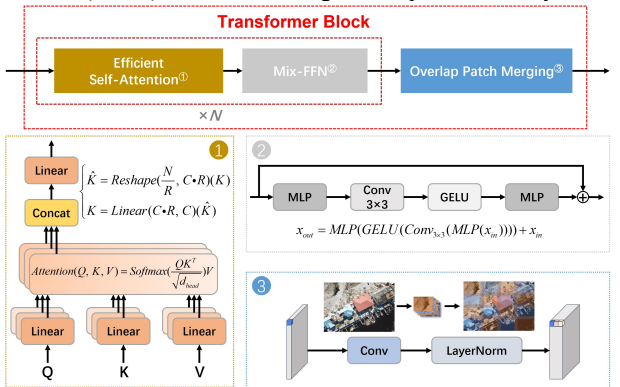


Figure 2. Structure of the Transformer block.

$$\begin{cases} \hat{K} = Reshape(\frac{N}{R}, C \times R)(K) \\ K = Linear(C \times R, C)(\hat{K}) \end{cases}$$
 (3)

Position-Encoding (PE) is commonly used in Transformer structures. In ViT, PE's resolution is fixed, meaning that when the image resolution changes, PE must also adjust, leading to decreased accuracy. The Mix-FFN addresses this by combining 3×3 convolution with MLP, effectively replacing PE.

$$x_{out} = MLP(GELU(Conv_{3\times3}(MLP(x_{in})))) + x_{in}$$
 (4)

Overlap Patch Merging is an image processing technique that merges overlapping image patches into a complete image. In image processing, dividing an image into smaller patches can reduce computational complexity and improve processing efficiency. However, when patches overlap, they must be merged to restore the image's integrity. The Overlap Patch Merging module retains the width and height of the input feature map while increasing the number of channels to capture contextual information. This helps the model capture context across different scales, thus improving its performance.

2.2 Disaster Damage Index (DDI): A New Metric for Disaster Severity

2.2.1 Definition and Weight Calculation of DDI: To objectively and accurately describe the disaster situation in different regions, we have designed a new metric called the Disaster Damage Index (DDI). The traditional method used by RescueNet for manual disaster classification lacks standardized norms and is limited by only three levels, which fail to cover the full range of disaster scenarios. To address this, DDI combines the proportion of damaged area of buildings and roads to provide a more reasonable disaster assessment approach. For each semantic-segmented UAV image, DDI is defined as follows:

$$DDI = \varphi \times \sum_{i=1}^{n} \frac{\Omega_{i} \times R_{i}}{W \times H}$$
 (5)

where k is a scaling factor used to adjust the value range of DDI, set to $\varphi = 10$ in this study; R_i represents the area of the i-th class of objects on the image; Ω_i denotes the importance weight of the i-th class of objects; W and H represent the width and height of the image, respectively.

The area of each class can be represented by the number of pixels, and the importance weights are calculated using the Analytic Hierarchy Process (AHP). AHP is an excellent semi-quantitative multi-criteria decision-making method used for structuring and making decisions on complex problems involving multiple criteria. It allows for the allocation of weights to different influencing factors. This method decomposes a complex overall ranking into multiple pairwise comparisons, generating a higher-order judgment matrix. Personal preferences of decision-makers are incorporated into the comparison process to quantify the importance of different influencing factors. The quantification standards are shown in Table 1.

Scale	Meaning	
1	Two elements are equally important	
3	The first element is slightly more important than	
3	the second	
5	The first element is clearly more important than the	
3	second	
7	The first element is extremely more important than	
/	the second	
9	The first element is strongly more important than	
9	the second	
2, 4, 6, 8	Intermediate values between adjacent judgments	
1-9	Importance when swapping the order of two	
reciprocal	elements	

Table 1. Importance Quantification Scale.

Based on this table, a judgment matrix A is generated, ensuring it meets the criteria for the characteristic root and eigenvector conditions: $A\Omega = \lambda_{\max} \Omega$. Here, the maximum eigenvalue of A is λ_{\max} , and the corresponding normalized eigenvector is Ω .

$$A = \begin{bmatrix} 1 & 1/a_{21} & \cdots & 1/a_{n1} \\ a_{21} & 1 & \cdots & 1/a_{n2} \\ \vdots & \vdots & \ddots & \vdots \\ a_{n1} & a_{n2} & \cdots & 1 \end{bmatrix}$$
 (6)

$$A\Omega = \lambda_{\max} \Omega \tag{7}$$

Once the weights Ω are computed, consistency checking is required. The main purpose of consistency checking is to ensure there are no logical issues in the construction of the judgment matrix. Pairwise comparisons in AHP can lead to logical inconsistencies, especially when the number of elements is large. For example, if the pairwise comparison results show A1>A2 and A2>A3, it should logically follow that A1>A3. If the judgment matrix incorrectly indicates A1<A3, this constitutes a logical issue. The consistency ratio (CR) is calculated using the following formulas, where CR<0.1 indicates that the weights are reasonable:

$$CI = \frac{\lambda_{\text{max}} - n}{n - 1} \tag{8}$$

$$CR = \frac{CI}{RI} \tag{9}$$

where n is the matrix order, and RI is the random consistency index derived from 1000 simulation experiments.

Adjusted Inverse Distance Weighting (AIDW): After 2.2.2 calculating DDI for all images, we obtain a series of spatially discrete points. To reflect the continuous variation in disaster severity with location, we introduce the Adjusted Inverse Distance Weighting (AIDW) method for spatial interpolation. This method is an improvement over the traditional Inverse Distance Weighting (IDW) technique and aims to address the IDW's limitations when dealing with uneven sample distributions. In IDW, samples located in one direction from the interpolation point may overshadow samples in other directions, reducing their influence. The AIDW method introduces an orientation-modulated weight coefficient to account for both the distance and directional relationships between samples and interpolation points, thereby improving the interpolation's accuracy.

Assuming that the result at any given point is influenced by the nearest n sample points (in this study, n = 10), the DDI for the interpolation point is calculated as follows:

$$DDI = \sum_{i=1}^{n} \frac{k_{i}}{(d_{i})^{p}} DDI_{i} / \sum_{i=1}^{n} \frac{k_{i}}{(d_{i})^{p}}$$
 (10)

where k_i is the orientation-modulated weight coefficient for the i-th sample point, representing the combined effect of overshadowing by other sample points; d_i denotes the Euclidean distance between the interpolation point Po and the i-th sample point; P is the power index reflecting the distance's impact, generally set to p=2; and DDI_i is the disaster damage index for the i-th sample point.

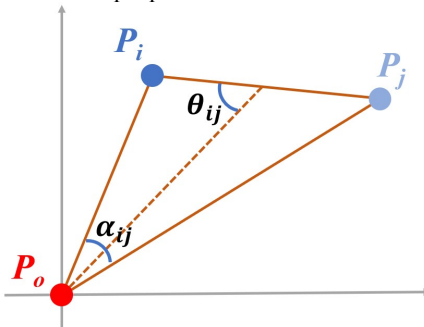


Figure 3. Schematic diagram of interpolation calculation.

The orientation-modulated weight coefficient k_i is computed as follows:

$$k_{i} = \begin{cases} 1 & i = 1\\ \prod_{j=1}^{j=i-1} \sin^{p} \theta_{ij} & i = 2, 3, \dots, n \end{cases}$$
 (11)

$$\sin^{p} \theta_{ij} = \begin{cases} 1 & \alpha_{ij} \geqslant 360^{\circ} / n \\ (1 - \cos^{2} \theta_{ij})^{\frac{p}{2}} & \alpha_{ij} < 360^{\circ} / n \end{cases}$$
(12)

where, $1 \le j \le i-1$, and the distance to the interpolation point is similarly constrained by $d_1 \le d_j \le d_{i-1}$. θ_{ij} represents the angle

(either acute or right) between the line connecting the two sample points $P_i P_j$ and the line connecting the interpolation point P_o with the midpoint of $P_i P_j$. α_{ij} is the angle formed between the lines connecting the sample points i and j with the interpolation point. The basic assumption of AIDW method suggests that when $\alpha_{ij} \ge 360^\circ/n$, the sample point j does not exert a shadowing effect on sample point i in the interpolation process.

This approach ensures that when certain spatial relationships between sample points and the interpolation point are met, the influence of one point on another is minimized or excluded, enhancing the accuracy of spatial interpolation.

3. Experiments and Results

3.1 Dataset and Evaluation Metrics

3.1.1 RescueNet: On October 10, 2018, Hurricane Michael made landfall near Mexico Beach as a Category 4 hurricane, becoming one of the strongest storms in the region's history. With wind speeds reaching up to 250 kilometers per hour, accompanied by powerful storm surges and torrential rainfall, the hurricane caused widespread destruction. A large number of houses were destroyed, critical infrastructure was severely damaged, and both power and communication systems were disrupted. The storm surge led to extensive coastal flooding, while heavy rainfall inland triggered severe waterlogging, further exacerbating the disaster's impact.

In the aftermath of the hurricane, the Center for Robot-Assisted Search and Rescue (CRASAR) conducted 80 UAV flights between October 11 and 14, 2018, capturing a large volume of high-resolution post-disaster imagery. Based on these images, Rahnemoonfar et al. manually annotated buildings, roads, and other objects across various levels of damage, resulting in a new dataset designed for computer vision applications—RescueNet (Rahnemoonfar et al., 2023). The dataset includes a total of 3,595 training images, 449 validation images, and 450 test images.

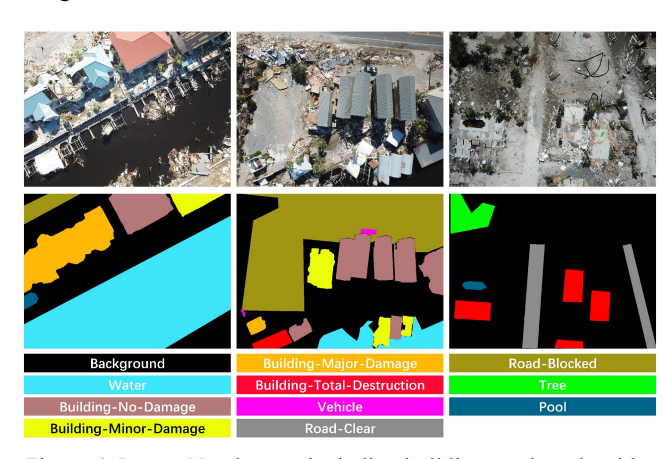


Figure 4. RescueNet dataset, including buildings and roads with varying damage levels.

3.1.2 Evaluation Metrics and Comparative Models: Common evaluation metrics for semantic segmentation models include average accuracy (aAcc), mean accuracy (mAcc), and mean Intersection over Union (mIoU). The aAcc measures the overall classification accuracy of the model, calculated as the ratio of correctly classified pixels to the total number of pixels. However, it does not account for class imbalance. In contrast, mAcc averages the classification accuracy across all classes, providing a better reflection of the model's ability to handle imbalanced categories. The mIoU, a widely used metric for assessing the overlap between predicted and ground truth regions, evaluates the model's performance in spatial localization and reveals its ability to accurately capture target

Under consistent training conditions, we compare the performance of H4DNet on the RescueNet dataset with several state-of-the-art semantic segmentation models, including DANet (Fu et al., 2019), PSPNet (Zhao et al., 2017), SegFormer (Xie et al., 2021), and UPerNet (Xiao et al., 2018).

3.2 Results

3.2.1 Performance Evaluation of H4DNet: The various accuracy metrics for the multiple models involved in the experiment are shown in Table 2.

	aAcc / %	mAcc / %	mIoU / %
DANet	93.09	86.25	75.74
PSPNet	93.80	86.58	76.78

Segformer	93.17	87.75	72.34
UPerNet	93.68	86.06	74.97
H4DNet	93.71	87.80	78.01

Table 2. Accuracy Comparison of Different Semantic Segmentation Models.

H4DNet outperforms other models in key metrics, particularly in mIoU with 78.01%, demonstrating superior pixel-level classification and spatial localization. Its high mIoU suggests better recognition of class boundaries, making it more effective in practical applications. While PSPNet leads in aAcc at 93.80%, it lags in mAcc and mIoU, scoring 86.58% and 76.78%, respectively. This indicates that PSPNet excels in pixel classification but struggles with imbalanced classes and spatial accuracy compared to H4DNet. SegFormer performs best in mAcc (87.75%), showing strength in class balance, but its mIoU of 72.34% reveals limitations in spatial localization, particularly with complex shapes. UPerNet, with an aAcc of 93.68% and mIoU of 74.97%, offers strong classification but falls short in spatial localization, while DANet's performance is more average, achieving an mIoU of 75.74%, reflecting difficulties in capturing boundaries and spatial relationships. Overall, H4DNet demonstrates the most balanced performance, excelling in critical spatial metrics.

Figure 5 presents partial results from the five models tested on the dataset, along with the corresponding original images and semantic segmentation masks. To facilitate observation, key areas are highlighted with red rectangles.

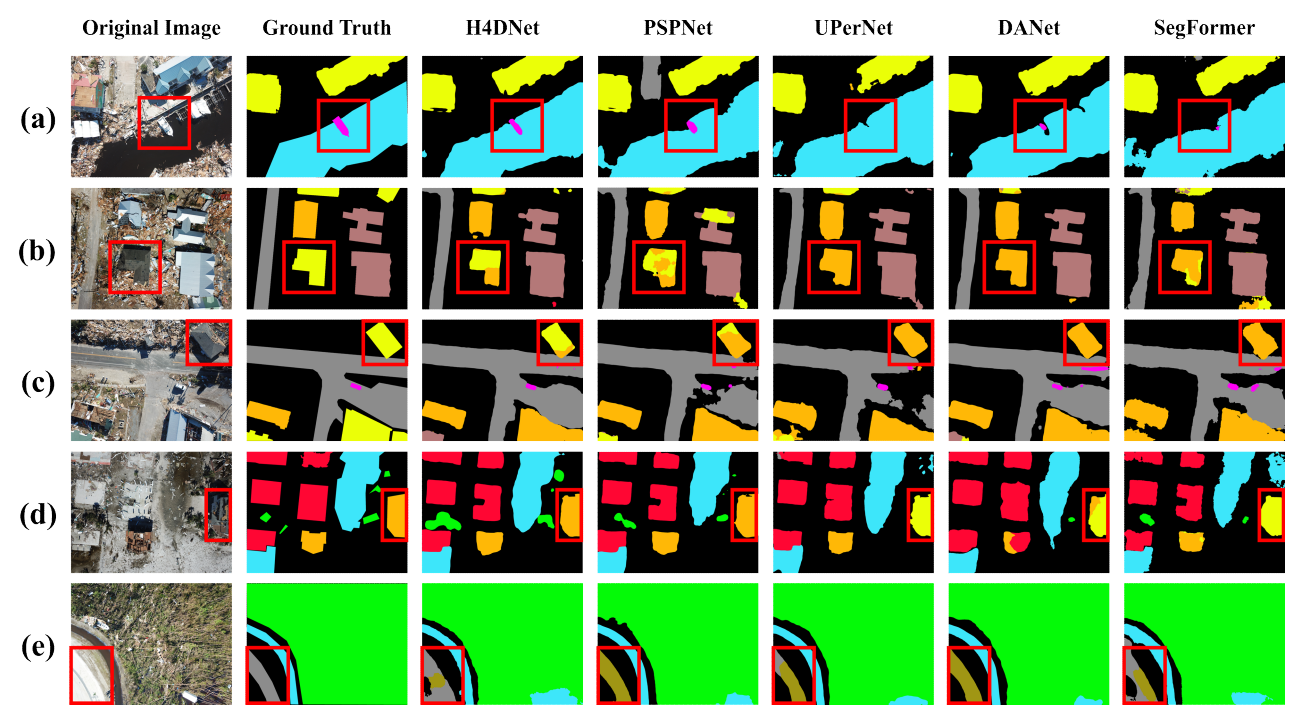


Figure 5. Semantic segmentation results for different models.

In panel (a), the highlighted regions reflect the model's performance on imbalanced classes, providing an evaluation of overall model performance. For example, the "vehicle" category, which has a small area and high similarity to the background, presents a significant challenge for differentiation. Among the five models tested, UperNet classifies the highlighted small boat completely as background; DANet and SegFormer identify only a part of the boat; PSPNet's segmentation is relatively better but

still lacks completeness compared to H4DNet. Additionally, beyond the highlighted areas, H4DNet shows superior segmentation of water bodies and buildings compared to the other models. Thanks to its advantages in mAcc and mIoU, H4DNet handles various land cover categories more comprehensively.

Panels (b), (c), (d), and (e) focus on the models' performance in distinguishing buildings and roads with different levels of damage, which is the core task of this study. In panels (b) and (c), the highlighted buildings are minor damaged, but UperNet, DANet, and SegFormer incorrectly classify them as major damaged. PSPNet and H4DNet manage to segment the minor damaged areas better, with H4DNet providing a more complete segmentation result. In contrast, panel (d) shows buildings initially classified as major damaged being mistakenly identified as minor damaged by models other than PSPNet and H4DNet. In panel (e), all five models struggle with distinguishing between clear and blocked roads, with PSPNet, UperNet, and DANet incorrectly classifying entire clear roads as blocked. H4DNet and SegFormer perform the segmentation with the highest accuracy. These results highlight the complexity of distinguishing between varying damage levels and different types of roads, with H4DNet showing the best adaptation to this task due to its highest mIoU.

In summary, H4DNet stands out for its balance and spatial precision, with a significant improvement in mIoU indicating its suitability for complex scene classification tasks. While PSPNet excels in average accuracy, it falls short in spatial precision. SegFormer, though strong in handling class imbalance, shows weaker spatial localization capabilities. UperNet and DANet perform reasonably well but do not surpass H4DNet in key metrics. Therefore, H4DNet demonstrates superior robustness and adaptability, suggesting broader potential in practical applications.

3.2.2 Analysis of DDI Spatial Distribution: In the calculation, categories that do not effectively reflect disaster conditions, such as "Building_No_Damage" and "Road-Clear," are assigned a weight of 0. For the categories of Building-Minor-Damage, Building-Major-Damage, Building-Total-Destruction, and Road-Blocked, we use the Analytic Hierarchy Process (AHP) for weight calculation. The importance judgment matrix we used is as follows:

	Building- Minor- Damage	Building- Major- Damage	Building- Total- Destruction	Road- Blocked
Building- Minor- Damage	1	1/5	1/9	1/3
Building- Major- Damage	5	1	1/5	3
Building- Total- Destruction	9	5	1	5
Road- Blocked	3	1/3	1/5	1

Table 3. The importance judgment matrix.

In evaluating importance, we considered Building-Minor-Damage < Road-Blocked < Building-Major-Damage < Building-Total-Destruction, leading to the above judgment matrix. The calculated weights for each category are:

Class	Weight
Building-Minor-Damage	0.047
Building-Major-Damage	0.213
Building-Total-Destruction	0.634
Road-Blocked	0.106

Others	0

Table 4. The calculated weights for each category.

The calculated Consistency Ratio (CR) is 0.068, which is less than 0.1, indicating that the weight setting is reasonable.

Based on this, the disaster situation spatial distribution obtained through interpolation is as shown in Figure 6. The Disaster Damage Index (DDI) exhibits a distinct spatial distribution pattern, with DDI values increasing as one approaches the coastline and gradually decreasing from northwest to southeast. This unique distribution pattern is closely related to the mechanism of Hurricane Michael. When Hurricane Michael made landfall on the Florida coast, the immense energy was initially released in the coastal areas, causing significant damage. As the hurricane moved inland, buildings, vegetation, and other terrain features along the way acted as buffers, weakening the storm's strength, which resulted in lower DDI values in the inland areas. Additionally, the topography within the study area significantly influenced the spatial distribution of the DDI. Notably, the elevation in the northwest of the study area is generally higher than in the southeast, with an elevation difference of nearly 20 meters. This elevation difference greatly determines the variation in hurricane impact. In the higherelevation northwest region, the storm surge and flooding caused by the hurricane are less likely to penetrate, resulting in lower DDI values. Conversely, the lower-elevation southeast region is more susceptible to storm surges and flooding, leading to higher DDI values.

-85°25'

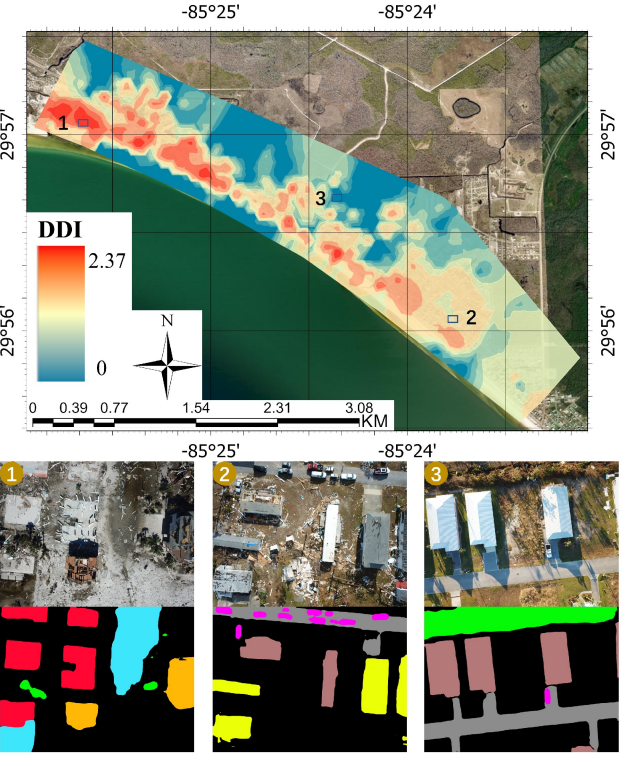


Figure 6. DDI spatial distribution map.

We selected three typical points from the figure according to DDI values, from highest to lowest, and displayed the corresponding UAV images and semantic segmentation results. First, the image at Location 1 shows numerous buildings that are total destroyed and some major damaged buildings, thus having the highest DDI value among the three points. Location 2 primarily contains minor damaged buildings, undamaged buildings, clear roads, and numerous parked cars. Compared to

Location 1, the disaster extent is significantly lighter, resulting in a lower DDI value. Location 3's image shows no damaged buildings or blocked roads, resulting in a DDI value of 0. Comparing these three sample points demonstrates that the proposed DDI indicator effectively and accurately reflects the overall disaster conditions in different areas, showcasing strong practicality and reliability.

3.2.3 Spatial distribution of features with different damage levels: The calculation of DDI primarily relies on four categories of land cover: Building-Minor-Damage, Building-Major-Damage, Building-Total-Destruction, and Road-Blocked. Figure 7 illustrates the spatial relative density distribution of these four categories, all computed using the AIDW algorithm for spatial interpolation. The spatial distribution patterns of these land cover types closely align with the final computed DDI values. In particular, the buildings classified as Building-Total-Destruction are densely concentrated in the northwest coastal region, which is closely related to the maximum weight assigned to this category in the DDI calculation.

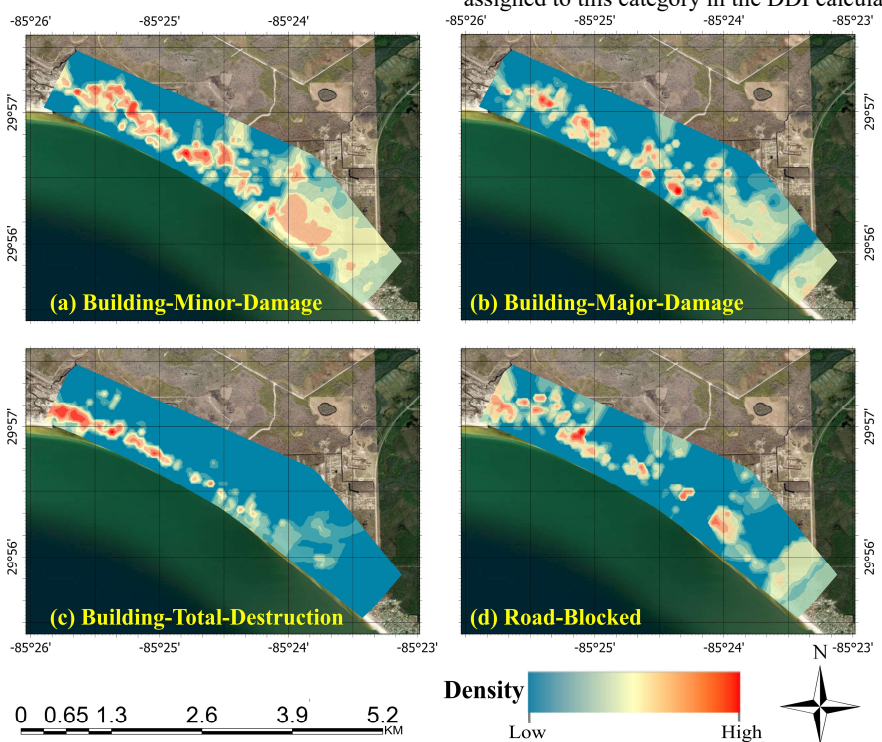


Figure 7. Spatial distribution of features with different levels of destruction.

Upon further examination of Figure 7, we observe an interesting phenomenon: compared to the other three categories, the spatial distribution of Building-Total-Destruction is more concentrated and primarily close to the coastline. In the direction extending from the coast inland within the study area, Building-Total-Destruction is almost restricted to the first one-third of the range, while the distribution of other categories is more widespread but decreases in density with increasing distance inland. Additionally, categories with lower damage levels have broader distribution ranges.

We attribute this phenomenon to the energy dissipation process of the hurricane after landfall. When a hurricane initially makes landfall, its energy is at its peak, causing the most severe damage, especially in coastal areas, where all categories of damaged land cover are present. Coastal land cover, while being destroyed, also absorbs some of the hurricane's energy. Therefore, buildings near the coast often experience the most severe destruction. As the hurricane progresses inland, its energy gradually dissipates, resulting in less extensive damage and a decrease in the number of total destroyed buildings. Further inland, the hurricane's energy weakens even more, reducing the extent of damage and altering land cover distribution.

Based on this observation, we recommend that coastal cities, when preparing for hurricane disasters, pay particular attention to defensive measures in coastal areas. For example, buildings should be reinforced with structures designed to withstand hurricanes to mitigate significant damage during initial landfall. Additionally, more disaster-resistant infrastructure, such as wind barriers or buffer zones, should be considered near the coastline to reduce the impact of hurricanes on inland buildings and infrastructure.

4. Conclusions

This study proposes a rapid assessment method for natural disaster damage based on drone imagery, addressing limitations in model accuracy and spatial distribution analysis of existing methods. By developing the H4DNet model, we achieved performance improvements in semantic segmentation tasks, allowing precise extraction of damaged land cover information from drone images. Additionally, we introduced the Disaster Damage Index (DDI), which calculates the area proportion of damaged land cover and uses the Adjusted Inverse Distance Weighting (AIDW) method to generate spatial distribution maps of disaster impact, accurately reflecting the damage across different regions. Experimental results demonstrate that H4DNet excels in various evaluation metrics, and the DDI index effectively complements the analysis of disaster spatial distribution, providing valuable scientific support for disaster assessment and mitigation efforts. This research not only opens new avenues for the application of drone imagery in disaster evaluation but also provides technical support for future post-disaster emergency responses.

Acknowledgements

This study was jointly supported by: (1) Major Science and Technology Special Projects and Key R & D Projects in Yunnan Province in 2024 (No. 202403ZC380001); (2) National Key Research and Development Program of China (No. 2023YFB3906102); (3) Natural Science Foundation of Hubei Province (No. 2022CFB773); and (4) the Chutian Scholar Program of Hubei Province.

References

- Cheng, C., Behzadan, A.H. and Noshadravan, A., 2024. Rapid and Automated Vision-Based Post-Disaster Building Debris Estimation. *Computing in Civil Engineering 2023-Resilience, Safety, and Sustainability*: 60-67.
- Cheng, J., Deng, C., Su, Y., An, Z. and Wang, Q., 2024. Methods and datasets on semantic segmentation for Unmanned Aerial Vehicle remote sensing images: A review. *ISPRS-J. Photogramm. Remote Sens.*, 211: 1-34.
- Chowdhury, T., Rahnemoonfar, M., Murphy, R. and Fernandes, O., 2020. Comprehensive Semantic Segmentation on High Resolution UAV Imagery for Natural Disaster Damage Assessment. 2020 Ieee International Conference On Big Data (Big Data): 3904-3913.
- Christidou, A.N., Drakaki, M. and Linardos, V., 2022. A Machine Learning Based Method for Automatic Identification of Disaster Related Information Using Twitter Data. *Intelligent and Fuzzy Systems: Digital Acceleration and the New Normal, Infus* 2022, Vol 2, 505: 70-76.
- Fan, Y., Wen, Q., Wang, W., Wang, P., Li, L. and Zhang, P., 2017. Quantifying disaster physical damage using remote sensing data—A technical work flow and case study of the 2014 Ludian earthquake in China. *Int. J. Disaster Risk Sci.*, 8: 471-488.
- Fu, J., Liu, J., Tian, H., Li, Y., Bao, Y., Fang, Z. and Lu, H., 2019. Dual Attention Network for Scene Segmentation. 2019 Ieee/Cvf Conference On Computer Vision and Pattern Recognition (CVPR 2019): 3141-3149.
- Guan, X. and Chen, C., 2014. Using social media data to understand and assess disasters. *Nat. Hazards*, 74: 837-850.
- Holail, S., Saleh, T., Xiao, X., Xiao, J., Xia, G., Shao, Z., Wang, M., Gong, J. and Li, D., 2024. Time-series satellite remote sensing reveals gradually increasing war damage in the Gaza Strip. *Natl. Sci. Rev.*, 11(9): nwae304.
- Jozi, D., Shirzad-Ghaleroudkhani, N., Luhadia, G., Abtahi, S. and Gül, M., 2024. Rapid post-disaster assessment of residential buildings using Unmanned Aerial Vehicles. *Int. J. Disaster Risk Reduct.*, 111: 104707.

- Mai, C., Wu, Y., Zhai, Y., Quan, H., Zhou, J., Genovese, A., Piuri, V. and Scotti, F., 2024. DBCG-Net: Dual Branch Calibration Guided Deep Network for UAV Images Semantic Segmentation. *IEEE J. Sel. Top. Appl. Earth Observ. Remote Sens.*, 17: 7932-7945.
- Markhvida, M., Walsh, B., Hallegatte, S. and Baker, J., 2020. Quantification of disaster impacts through household well-being losses. *Nat. Sustain.*, 3(7): 538-547.
- Opper, I.M., Park, R.J. and Husted, L., 2023. The effect of natural disasters on human capital in the United States. *Nat. Hum. Behav.*, 7(9): 1442-1453.
- Rahnemoonfar, M., Chowdhury, T. and Murphy, R., 2023. RescueNet: A high resolution UAV semantic segmentation dataset for natural disaster damage assessment. *Sci. Data*, 10(1): 913
- Raja, G., Manoharan, A. and Siljak, H., 2024. Ugen: Uav and gan-aided ensemble network for post-disaster survivor detection through oran. *IEEE Trans. Veh. Technol.*, 73(7): 9296-9305.
- Ritchie, H., Rosado, P. and Roser, M., 2022. *Natural Disasters. Our World in Data*.
- Robinson, C., Nsutezo, S.F., Ortiz, A., Sederholm, T., Dodhia, R., Birge, C., Richards, K., Pitcher, K., Duarte, P. and Ferres, J.M.L., 2023. Rapid building damage assessment workflow: An implementation for the 2023 Rolling Fork, Mississippi tornado event. 2023 Ieee/Cvf International Conference On Computer Vision Workshops, Iccvw: 3762-3766.
- Ronneberger, O., Fischer, P. and Brox, T., 2015. U-Net: Convolutional Networks for Biomedical Image Segmentation. *Medical Image Computing and Computer-Assisted Intervention, Pt III*, 9351: 234-241.
- Schaefer, M., Teeuw, R., Day, S., Zekkos, D., Weber, P., Meredith, T. and Van Westen, C.J., 2020. Low-cost UAV surveys of hurricane damage in Dominica: automated processing with co-registration of pre-hurricane imagery for change analysis. *Nat. Hazards*, 101(3): 755-784.
- Xiao, T., Liu, Y., Zhou, B., Jiang, Y. and Sun, J., 2018. Unified Perceptual Parsing for Scene Understanding. *Computer Vision Eccv 2018*, *Pt V*, 11209: 432-448.
- Xie, E., Wang, W., Yu, Z., Anandkumar, A., Alvarez, J.M. and Luo, P., 2021. SegFormer: Simple and efficient design for semantic segmentation with transformers. *Advances in Neural Information Processing Systems*, 34: 12077-12090.
- Zhao, H., Shi, J., Qi, X., Wang, X. and Jia, J., 2017. Pyramid Scene Parsing Network. *30Th Ieee Conference On Computer Vision and Pattern Recognition (CVPR 2017)*: 6230-6239.
- Zhengquan, L., Kuo, W., Hao, M. and Yaoxiang, W., 2018. An Adjusted Inverse Distance Weighted Spatial Interpolation Method, *Proceedings of the 2018 3rd International Conference on Communications, Information Management and Network Security (CIMNS 2018)*. Atlantis Press, pp. 128-132.